Time dependent stability margin in multistable systems

P. Brzeski, J. Kurths, and P. Perlikowski

Citation: Chaos **28**, 093104 (2018); doi: 10.1063/1.5042310
View online: https://doi.org/10.1063/1.5042310
View Table of Contents: http://aip.scitation.org/toc/cha/28/9
Published by the American Institute of Physics

Time dependent stability margin in multistable systems

P. Brzeski,[1,a)] J. Kurths,[2,3,b)] and P. Perlikowski[1,c)]
[1]*Division of Dynamics, Lodz University of Technology, 90-924 Lodz, Poland*
[2]*Potsdam Institute for Climate Impact Research, Potsdam 14415, Germany*
[3]*Institute of Physics, Humboldt University of Berlin, Berlin 12489, Germany*

(Received 31 May 2018; accepted 22 August 2018; published online 10 September 2018)

We propose a novel technique to analyze multistable, non-linear dynamical systems. It enables one to characterize the evolution of a time-dependent stability margin along stable periodic orbits. By that, we are able to indicate the moments along the trajectory when the stability surplus is minimal, and even relatively small perturbation can lead to a tipping point. We explain the proposed approach using two paradigmatic dynamical systems, i.e., Rössler and Duffing oscillators. Then, the method is validated experimentally using the rig with a double pendulum excited parametrically. Both numerical and experimental results reveal significant fluctuations of sensitivity to perturbations along the considered periodic orbits. The proposed concept can be used in multiple applications including engineering, fluid dynamics, climate research, and photonics. *Published by AIP Publishing.* https://doi.org/10.1063/1.5042310

Multistability is commonly met in dynamical systems originating from various disciplines including control engineering, networks, fluid dynamics, biology, photonics, neurobiology, and nonlinear dynamics. Due to the coexistence of stable attractors, we observe sudden changes in dynamical response. An important real-life example is a circadian clock. Recent studies suggest that it is far safer to undergo heart surgery in the afternoon than in the morning. Also, heart attacks and strokes are more probable in the morning. Those events take place in a different moment of a circadian clock; hence, we can say that in the afternoon the stability margin is larger, while in the morning it shrinks and our body is more peril to dangerous incidents. The second example is systems with control which are commonly met in all fields of physics and engineering. The costs of control can be minimized by applying a controlling impulse in the appropriate moment. In mechanical and civil engineering to improve reliability and work safety of machines and structures, we should be able to detect parts of the working regime that determine its robustness. We propose a novel technique to characterize the time-dependence of stability margin along a stable trajectory. For that purpose, we analyze the changes in the minimum distance between the trajectory and the closest tipping points. We propose different measures to quantify this distance and the stability surplus. Our method enables one to expand the knowledge about the overall structure and compactness of the phase space of dynamical systems. The method implements a straightforward sample-based analysis and can be applied to a wide range of dynamical models. Moreover, one can utilize different stability margin indicators that best suit the considered phenomena. We explain the approach using two paradigmatic dynamical systems and verify the robustness of the technique with an experimental investigation of a double pendulum excited parametrically. Both numerical and experimental results reveal significant fluctuations of sensitivity to perturbations along the considered attractors which prove the usefulness of the method.

I. INTRODUCTION

Multistability is commonly met in dynamical systems originating from various disciplines including mechanical, civil and control engineering, fluid dynamics, biology, photonics, and statistical physics. Due to the coexistence of stable attractors, we observe sudden changes in dynamical response. However, all dynamical stability measures refer to the whole trajectory or one particular moment of time. Thus, they miss a crucial property of all dynamical systems: the existence of time-dependent susceptibility to perturbations along the orbit. Due to this feature, a given perturbation may or may not lead to a tipping point mainly depending on when it occurs. The idea is schematically presented in Fig. 1. The ball rolls along the grooved track, so its motion is locally stable. However, we see that in position 1 the ball is much more likely to reach the tipping point and jump to another regime than in position 2. Thus, it is extremely important where along the orbit a perturbation occurs.

Currently known methods provide the knowledge about a local stability of solutions of a dynamical system. The stability of equilibria is defined using eigenvalues.[18] The Floquet theory lets us calculate the stability of periodic solutions.[13] In the case of quasi-periodic motion, it is a more challenging task. Analytically, we can determine the stability in simple cases, but with the support of numerical methods, the analysis can be done for all systems.[9,12,14] In the aforementioned cases, the stability is calculated only in a close neighborhood of the considered orbit. But when a multistable system is subjected to perturbations, it can evolve to a different coexisting solution. Thus, we should gain better insight into stability in a wider

[a)]Electronic mail: piotr.brzeski@p.lodz.pl
[b)]Electronic mail: kurths@pik-potsdam.de
[c)]Electronic mail: przemyslaw.perlikowski@p.lodz.pl

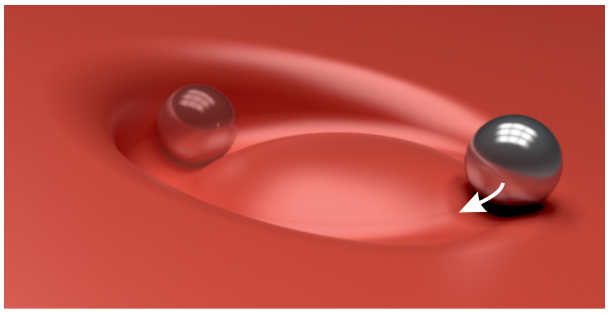

FIG. 1. Schematic presentation of the different susceptibility to perturbations along the orbit. The ball rolls around the track. This solution is asymptotically stable. Depending on the position of the ball, reaching tipping point is more (position 1) or less likely (position 2).

range of the phase space, which can be achieved by analyzing the basins of attraction.[3,10,32]

For systems with two dimensional phase space, basins of attraction show all solutions, as the behavior of the system depends only on two initial conditions. Thus, in such systems, we can perform a straightforward analysis and obtain detailed information about the phase space structure. When the phase space has three or more dimensions, we can just look into two-dimensional cuts of the multi-dimensional phase space. To overcome this problem, some new methods of analysis have been developed. Thompson *et al.*[19,30,31] proposed the concept of monitoring erosion of basins of attraction using a Poincaré map. Also, Rega and Lenci developed this concept and introduce different measures[20,21,26] which enable one to assess the structure of the basins of attraction. Still, these methods provide measures for the whole solutions but do not describe the evolution of stability margin along the orbit. Apart from that, due to the two-dimensional presentation limit of basins of attraction, these methods are hard to be applied for high-dimensional systems. The method "basin entropy" proposed by Daza *et al.*[7,8] provides an efficient algorithm to test the structure of basins of attraction and obtain information about its fractality.

In this paper, we propose a sample-based method that is paradigmatically similar to "basin stability" measure developed by Menck *et al.*[24] It enables one to quantify stability based on the probability of reaching a given attractor from random initial conditions. To estimate basin stability, one has to perform a significant number of Bernoulli trials and classify the final solution reached in each trial. This suprisingly simple quantifier has been already utilized in numerous applications. The first paper that used this idea shows the analysis of the synchronizability of Watts–Strogatz networks consisting of paradigmatic Rössler oscillators.[24] In Ref. 28, the relationship between stability against large perturbations and topological properties of a power transmission grid has been analyzed. The main advantage of the proposed algorithm is that it can be applied during live operation of a power grid to increase safety of the network. Then, the basin stability method has been used to identify three mechanisms which create the circulating power flows.[6] Additionally, the problem of efficiency increase of power grids has been considered with basin stability method in few more studies.[1,2,15,16,27]

The basin stability is also an efficient tool to analyze synchronization[23] or investigate the explosive transitions between synchronous and non-synchronous states[33] in large networks of oscillators. It can also be used to consider synchronized state in time-varying complex networks.[17] The interesting application of the basin stability method to systems with time delay has been presented in Ref. 22 and to piecewise and discontinuous systems (Amazonian vegetation model,[25] externally forced oscillator with impacts,[4] and system with dry friction[11]).

We have recently proposed an extension of this method,[4,5] where in addition to initial conditions, we draw the values of system parameters. Such an approach lets us include in the analysis the uncertainty of parameters or investigate systems with varying parameter values. Nevertheless, all aforementioned methods do not take into account the changes of basins during system time evolution.

In this paper, we include the time evolutions of the phase space structure and propose a robust sample-based method to characterize the time-dependent susceptibility to perturbations. With the method, we can identify crucial parts along the orbits where we are closest to tipping points and even small perturbation can induce a sudden event. The proposed method lets us detect changes in the distance to the closest margin of stability, hence all points that influence the phase space structure are taken into account and can be detected. The method can be applied to a wide range of dynamical models and one can utilize different stability margin indicators that best suit the considered phenomena. We explain this technique using two paradigmatic dynamical systems, i.e., the Rössler (autonomous) and Duffing (non-autonomous) oscillators. The evolution of an autonomous system is time-invariant, while for a non-autonomous oscillator, the resulting response is governed by a time-dependent function. Hence, for the two considered cases, we use two different approaches. However, in both models, we indeed find a volatility of susceptibility to perturbations. Finally, the robustness of the technique is validated experimentally for a double pendulum excited parametrically. Our investigations confirm different sensitivity to perturbations along the considered attractors which proves the usefulness of the method.

II. COMPUTATIONAL ALGORITHM

We propose a new method to describe the stability surplus along asymptotically stable periodic attractors. Instead of indicating the properties of the whole solution using an overall measure, we characterize the stability margin along the orbit—within one full period of motion. For that purpose, we analyze the changes in the minimum distance between the point on the orbit and the closest tipping point given as the adjacent boundary of the basin of attraction. We need a quantitative measure, such as a Euclidean distance in the phase space, the difference in the energy level, or different specific quantity related to the investigated phenomenon. Analyzing the changes of this measure, one can indicate the parts of the stable periodic orbit which are "more" or "less" susceptible to perturbations and find moments of the orbit where we are closest to a tipping point.

In the algorithm, we use the minimum Euclidean distance in the phase space between the current position on the attractor and the boundary of its basin of attraction. The proposed concept is general and can be applied for a wide range of dynamical systems. However, to maintain the physical meaning of the results, we should apply different procedures for autonomous and non-autonomous systems. The reason for this will be explained using archetypal 2-dimensional systems.

Let us assume that the considered system is multistable and has a periodic solution and is given by the coordinates (x, y). Two points (x_1, y_1) and (x_2, y_2) belong to the considered periodic attractor of period 2π presented in Fig. 2. At the time t_0, the system is in the point (x_1, y_1) and we perturb it so that it jumps to (x_2, y_2). If the system is autonomous [Fig. 2(a)], it will continue the motion along the attractor starting from (x_2, y_2), and the only effect of the perturbation is a shift in the phase. But, if the considered system is non-autonomous [Fig. 2(b)] after the perturbation, the system can reach a different attractor. Therefore, in non-autonomous systems, the perturbation has to be considered in the time domain, whereas for autonomous systems, we only care about the state of the system after the perturbation. We apply a sample-based approach to analyze effects of random perturbations along an attractor; hence, we must differentiate the procedure for autonomous and non-autonomous systems.

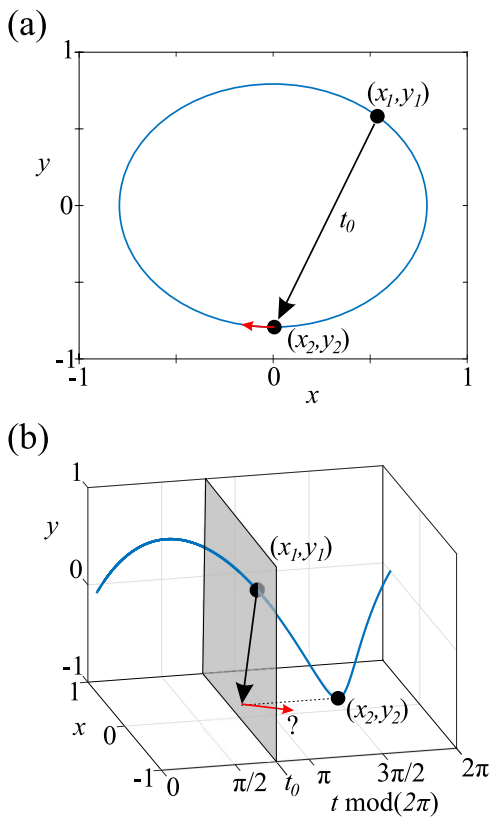

FIG. 2. Presentation of the exemplary periodic attractor of a 2-dimensional autonomous (a) and a non-autonomous (b) system. Both points (x_1, y_1) and (x_2, y_2) belong to the attractor. The black arrows indicate the effects of perturbation that occurs at time t_0.

A. Autonomous systems

The considered n-dimensional autonomous system is given as

$$\frac{dQ}{dt} = F(Q), \tag{1}$$

where $Q = (q_1, q_2, \ldots, q_n)$ is a vector of generalized coordinates that describes the state of the system. Let us assume that the system has a stable periodic attractor A and at least one different coexisting attractor. A has period T and can be presented as a curve in the n-dimensional Euclidean phase space. The length of this curve is given by the following formula:

$$L(A) = \int_0^T |F(Q)|dt. \tag{2}$$

Then, to characterize the stability margin along A, the following steps should be applied:

1. Discretize the investigated orbit into k segments of equal length $L(A)/k$.
2. For each segment, mark down the state of the system in the middle of this segment receiving k vectors $\left(q_1^i, q_2^i, \ldots, q_n^i\right)$, for $i = 1, 2, \ldots, k$.
3. Perform a series of m Bernoulli trials of direct numerical integration. In each trial, draw the values of the initial conditions and check if the system reaches A or a different attractor. After each trial, note the values of the initial conditions and whether A was reached.
4. For each segment, find the minimum Euclidean distance between its middle state and the initial conditions leading to a different attractor. By that, for each segment i, calculate the estimator D^i of the minimal distance between the attractor and the adjacent boundary of its basin of attraction.

The above procedure is presented schematically in Fig. 3 on the basis of a 3-dimensional autonomous system. Panel (a) shows a periodic attractor and the sample segments marked with different colors. We also indicate points that represent the states of the system in the middle of each segment given by the vectors $\left(q_1^1, q_2^1, q_3^1\right)$, $\left(q_1^2, q_2^2, q_3^2\right)$, etc. In panel (b), we present the 3-dimensional projections of the basins of attraction calculated around the middle point of the first segment $\left(q_1^1, q_2^1, q_3^1\right)$—in the planes q_1–q_2, q_2–q_3, and q_1–q_3. In panel (c), we show the zoom up around the point $\left(q_1^1, q_2^1, q_3^1\right)$ and the minimum distance from that point to the adjacent boundary of its basin of attraction given by the measure D^1.

B. Non-autonomous systems

The considered n-dimensional non-autonomous system is given as

$$\frac{dQ}{dt} = F\left(Q, t\right), \tag{3}$$

where $Q = q_1, q_2, \ldots, q_n$ is a vector of generalized coordinates that describes the state of the system. This system has a stable periodic attractor A and at least one different coexisting attractor. A has period T and can be presented as a curve in n-dimensional Euclidean phase space. The length of this

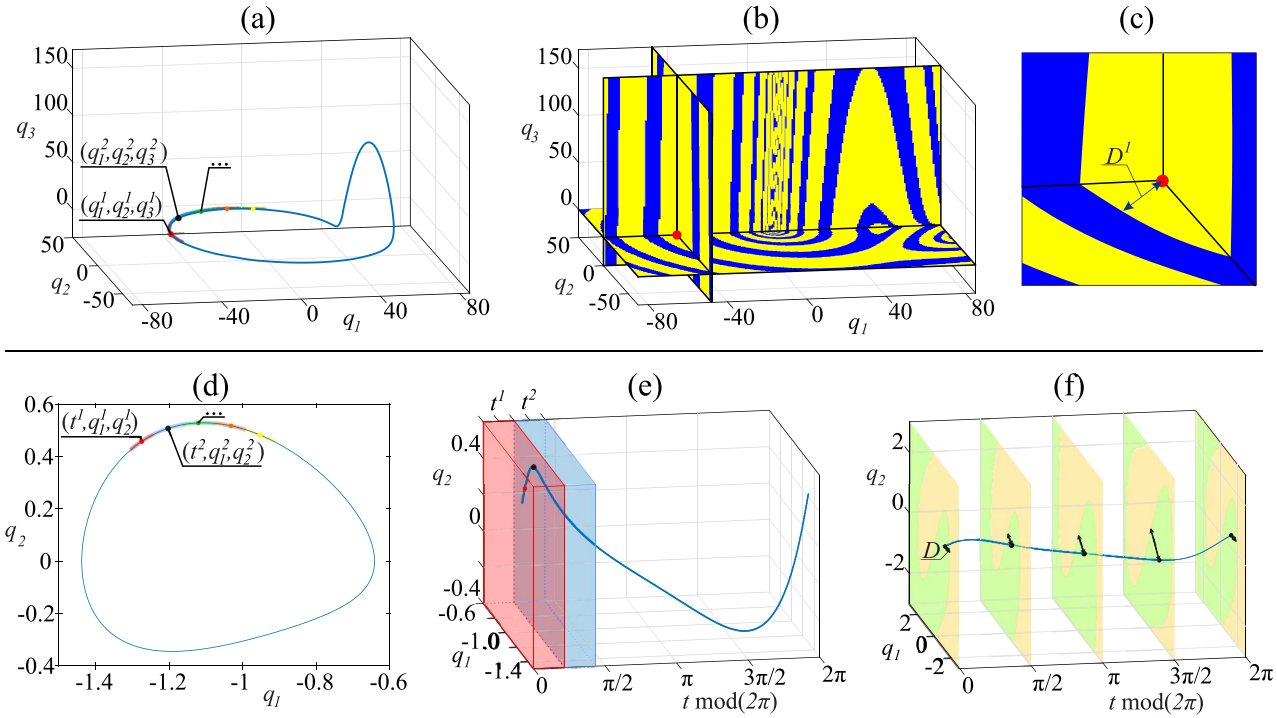

FIG. 3. Presentation of the procedure for an autonomous 3-dimensional system [(a)–(c)] and a 2-dimensional non-autonomous system [(d)–(f)]. Panels (a) and (d) show the considered attractors and sample segments with corresponding state vectors. Panel (b) presents the projections of the basins of attraction calculated for the point (q_1^1, q_2^1, q_3^1). Panel (c) is the zoom up around the point (q_1^1, q_2^1, q_3^1) on which we indicate measure D^1 for the first segment with navy arrow. Panel (e) presents the non-autonomous attractor in 3D space including time and parts of the phase space that refers to the first (red) and the second (blue) group of trials. Panel (f) shows the evolution of measure D depicted by navy arrows.

curve is given by the following formula:

$$L(A) = \int_0^T |F(Q,t)|dt. \tag{4}$$

Then, to characterize the stability margin along attractor A, the following steps should be applied:

1. Discretize the investigated orbit into k segments of equal length $L(A)/k$.
2. For each segment, mark down the initial time t_0^i and state of the system in the middle of the segment receiving k vectors $(t_0^i, t^i, q_1^i, q_2^i, \ldots, q_n^i)$, for $i = 1, 2, \ldots, k$, where $t_0^i = t \bmod T$ and $t^i = t \bmod T$.
3. Perform a series of m Bernoulli trials of direct numerical integration. In each trial, draw the values of the initial conditions and the initial time t_0 from the range $[0, T]$; then, check if the system reaches A or a different attractor. After each trial, note the values of initial conditions, initial time, and whether A was reached.
4. Divide all trials into k groups based on the initial time t_0. The trial belongs to group i if $t_0 \in [t_0^i, t_0^{i+1}]$, for $i = 1, 2, \ldots, k-1$ and $t_0 \in [t_0^k, T]$ for $i = k$.
5. For each segment, find the minimum Euclidean distance between its middle state and the initial conditions leading to a different attractor. During analysis of segment i, consider only trials that belong to i group. By that, for each segment i, we calculate the estimator D^i of the minimal distance between the attractor and the adjacent boundary of its basin of attraction.

The above procedure is presented schematically in Fig. 3 on the basis of a 2-dimensional non-autonomous system. In panel (d), we show the phase portrait of A and sample segments marked with different colors. We indicate points that represent the states of the system in the middle of each segment given by the vectors (t^1, q_1^1, q_2^1), (t^2, q_1^2, q_2^2), etc. In panel (e), we present the attractor in 3-dimensional view including time. This enables one to show the part of the phase space that includes the initial conditions belonging to the first (red) and the second (blue) group of trials. Panel (f) schematically indicates the evolution of measure D along the attractor (given by navy arrows).

C. General remarks

There are some general rules about the described procedures. Firstly, the more segments we use (the larger k), the more accurate description of the stability margin along the attractor we can provide. However, in practical applications, the choice of segmentation can be done based on the properties and restrictions imposed on the investigated system. For example, if we measure the angular position of the pendulum with 1 (deg) step, we should adjust the number of segments taking into account the measurement precision.

Similarly, the larger the number of trials m, the more accurate results we get. The minimum number of trials depends on the dimension of the considered system n and the number of segments k. In general, m should be greater than $10^n \cdot k$, but the minimum number of trials should also take into account the properties of investigated problem.

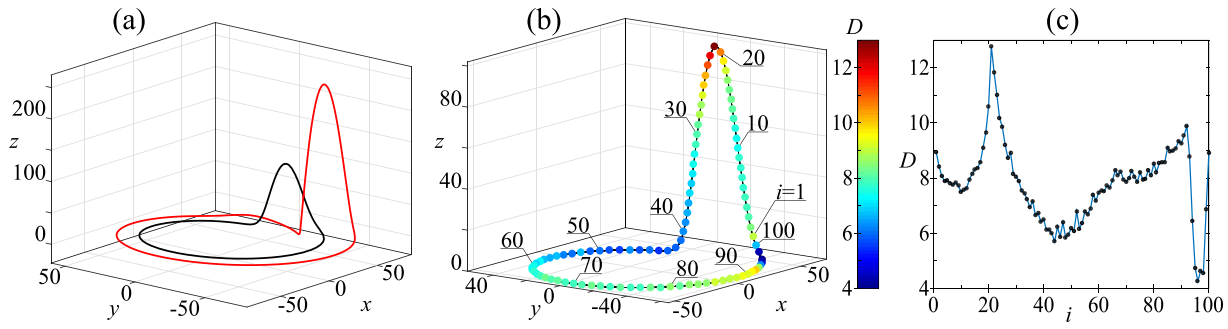

FIG. 4. Presentation of coexisting periodic attractors B (black line) and C (red line) of the Rössler system given by Eq. (5)—panel (a). Panel (b) shows attractor B with middle points of 100 segments marked by dots colored according to the value of D. Panel (c) presents the evolution of the stability margin D along the attractor B with respect to the number of segments.

In the description, we use the Euclidean distance as a measure between the orbit and the boundary of its basin of attraction. This measure has no physical meaning other than that it enables one to compare different parts of the orbit. As mentioned, the proposed concept is general and one can use other measures adequate for the considered phenomena, such as the difference in the energy level or a specific type of perturbation.

The results can be presented in the plot showing the changes of the selected measure (D) with respect to the number of segments, time, or one coordinate of the system. However, the aim is to provide a quantitative description of the stability margin along a stable periodic orbit. In the case of fractal basin, the distance will go to zero with a sufficient number of trials. Thus, one can use our method to identify attractors with fractal basin, but the distance will be the only obtained information. Based on that data, we can detect the position on the attractor with the minimum D_{MIN} and maximum D_{MAX} distance between the attractor and its basin boundary. D_{MIN} indicates the moment in which it is the easiest to induce the switch to another solution, while for D_{MAX} a transition to another attractor is the least likely to happen. Apart from the above, we can calculate the average distance between the attractor and the boundary of its basin of attraction along the attractor D_{AVG} which can help to compare the stability of co-existing attractors and provide crucial knowledge about the probability reaching tipping points.

III. PARADIGMATIC EXAMPLES

A. Rössler system—example of an autonomous system

As the first example, we consider the autonomous Rössler system given by the following set of ordinary differential equations (ODEs):

$$\begin{aligned} \dot{x} &= -y - z, \\ \dot{y} &= x + ay, \\ \dot{z} &= b + z\,(x - c)\,, \end{aligned} \tag{5}$$

with the following parameter values: $a = 0.2$, $b = 9.0$, $c = 48.0$, for which there exist two stable attractors (periodic oscillations) named B and C [Fig. 4(a)]. We will consider the time-dependent stability margin along the attractor B and divide it into $k = 100$ segments. We perform $m = 2\,000\,000$ trials each time randomly choosing initial conditions from the following ranges: $x \in [-85, 85]$, $y \in [-80, 60]$, $z \in [-30, 270]$. For each trial, we note initial conditions and remove some initial part to be on an attractor. Then, for each segment $i \in k$, we calculate the minimum distance D from its middle point to the initial conditions that do not lead to B. The results are presented in Figs. 4(b) and 4(c) where we show changes of D with respect to the number of segment i. In Fig. 4(b), we indicate the middle points for every segment with a dot using color scale to reflect the value of D. To enable the location of segments, we name every tenth segment. In Fig. 4(c), we show the results (black dots) and connect them to get the estimated $D(i)$ function. We find that

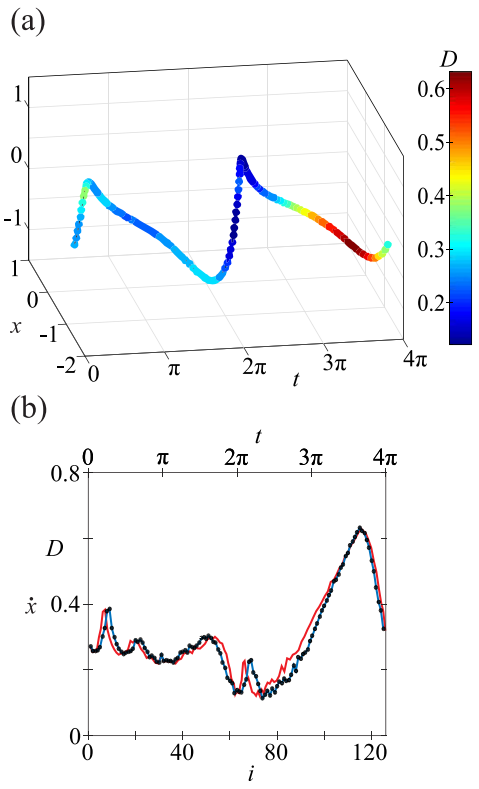

FIG. 5. Attractor F of the Duffing system [Eq. (6)] with middle points of 125 segments marked by dots colored according to the value of D—panel (a). Evolution of the stability margin D along attractor F with respect to the number of segments. With black dots, we indicate the value of D in the middle of segment and with blue line its continuous estimation (b).

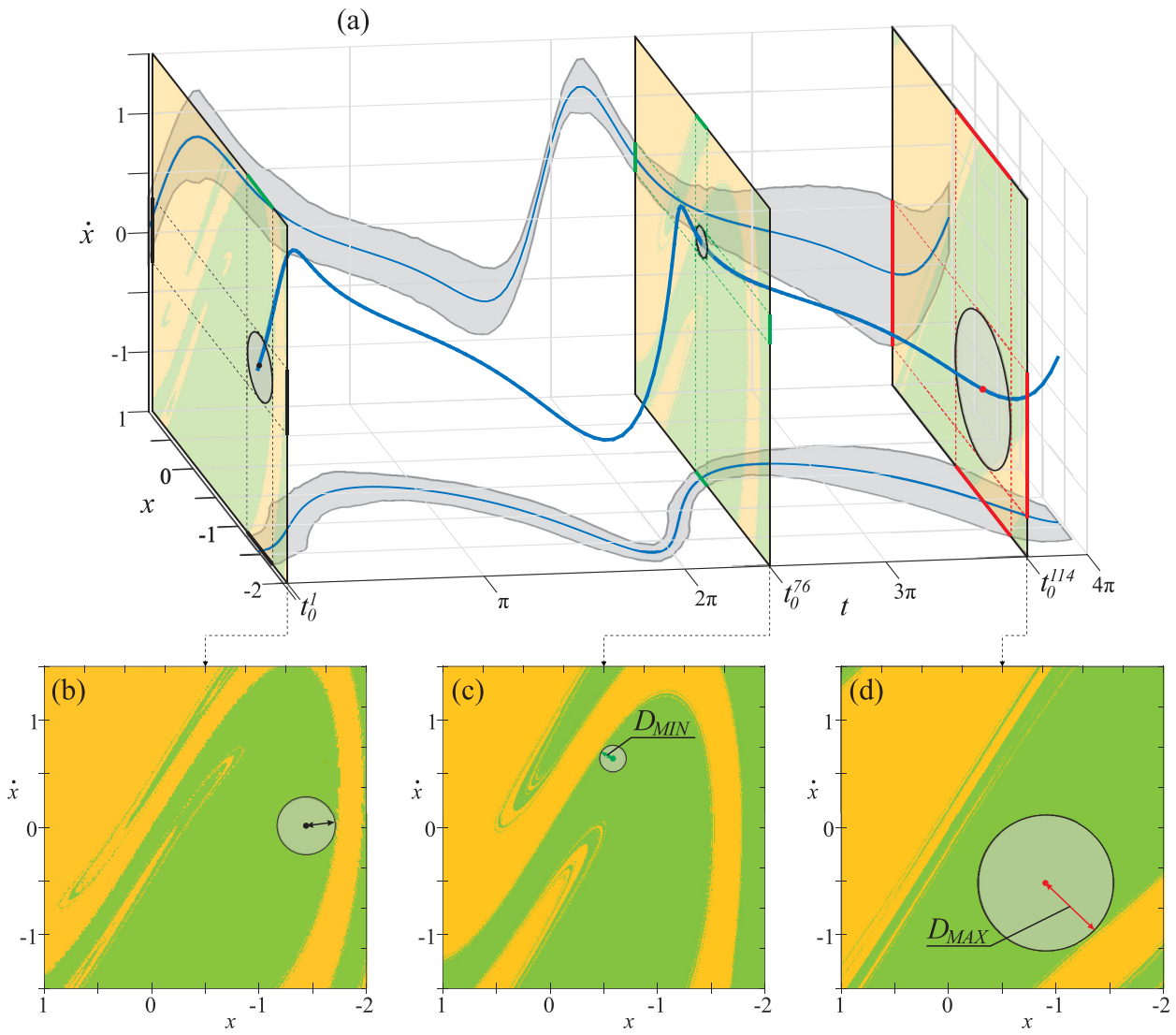

FIG. 6. Panel (a) is a 3D presentation of solution F with the evolution of measure D in time domain. Three exemplary basins of attraction calculated for t^1, t^{76}, and t^{114} are shown in panels (b), (c), and (d), respectively.

the value of D strongly varies along the considered attractor. It reaches its maximum value (12.77) for the 21st segment and its minimum (4.27) for the 96th segment. Generalizing, we can say that for most of the orbit $D \approx 8$, while it significantly increases when $z > 95$ and decreases for $z \in [0.5, 5]$. Thus, the stability margin substantially depends on the position of the attractor, and using the proposed method, we can indicate moments when reaching tipping point is more (low D) or less probable (high D).

B. Parametrically driven Duffing oscillator—example of a non-autonomous system

Next, we study the parametrically driven Duffing oscillator, a non-autonomous system given by the following second order ODE :

$$\ddot{x} + c\dot{x} - x + a\,[1 + f\,\sin(t)]\,x^3 = 0. \tag{6}$$

We use the following values of parameters: $c = 1$, $a = 1$, $f = 0.86$ for which there are two stable coexisting attractors F and G both corresponding to period-2 oscillations. Both attractors have the period 4π. We focus on the attractor F and divide it into $k = 125$ segments. We perform $m = 500\,000$ trials drawing initial conditions and time from the following ranges: $x \in [-3, 3]$, $\dot{x} \in [-3, 3]$, and $t_0 \in [0, 4\pi]$ as we analyze an attractor of period 4π. Then, we divide the trials in 125 groups based on the drawn initial time. In Fig. 5, we present the outcome of the procedure. Figure 5(a) presents with the color scale the evolution of D along the attractor in 3D space. In Fig. 5(b), we show the evolution of D with respect to the number of segments. The average distance to the basin boundary is $D_{AVG} = 0.295$, and we see that it varies noticeably along the attractor. The value of D oscillates around 0.3 for the first 45 segments, then it drops around the 75th segment, and increases up to 114th segment when it reaches its maximum value.

In Fig. 6(a), we present the evolution of distance between the F and the boundary of its basin of attraction in 3D space. The blue line is the trajectory of the system. On both the bottom and the back surfaces of the 3D panel (a), we show the projections of the trajectory as a blue curve and with gray color and we mark the projection of the "safe" part of the

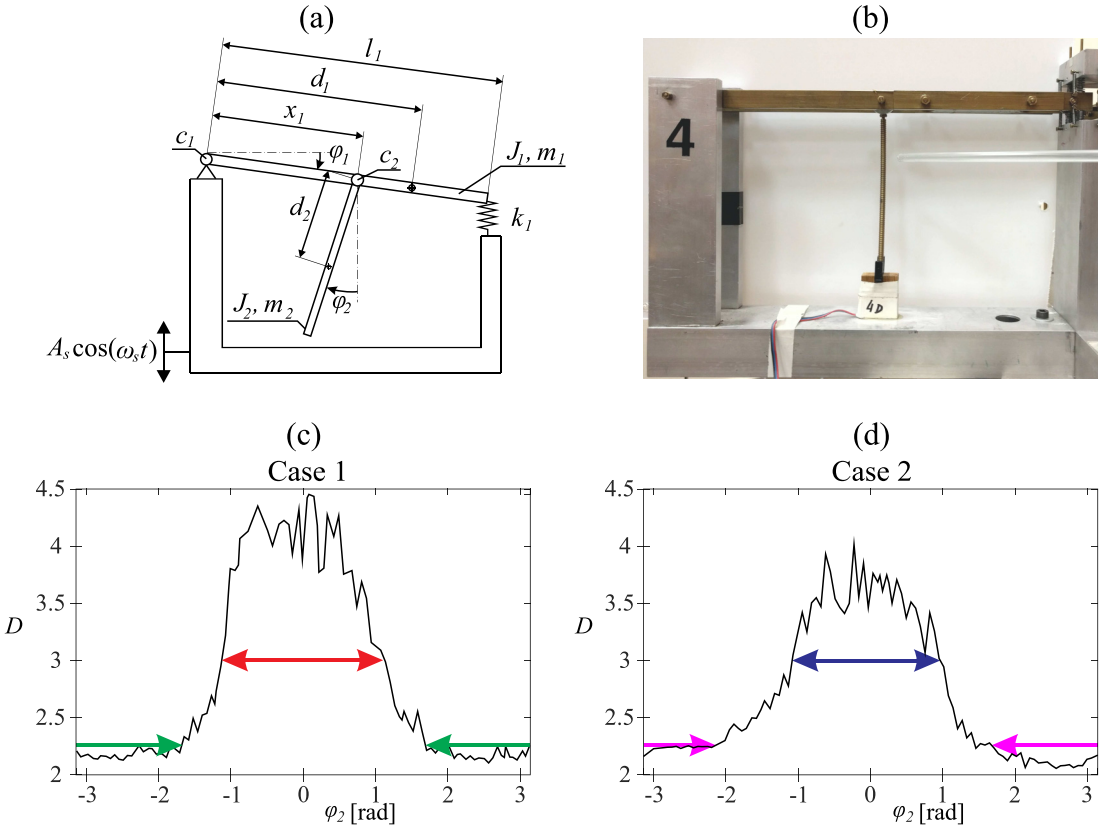

Experimental results				
direction of air flow (perturbation effect)	avg. pressure causing solution change [MPa] (nozzle position)			
	Case 1		Case 2	
	$\varphi_2 \approx 0$ [rad]	$\varphi_2 \approx \pi$ [rad]	$\varphi_2 \approx 0$ [rad]	$\varphi_2 \approx \pi$ [rad]
locally decreasing $\dot{\varphi}_2$	0.117 (5)	0.069 (2)	0.103 (5)	0.076 (2)
locally increasing $\dot{\varphi}_2$	0.219 (1)	0.145 (6)	0.179 (1)	0.132 (6)
locally decreasing $\dot{\varphi}_2$	0.234 (7)	0.165 (4)	0.200 (7)	0.159 (4)
locally increasing $\dot{\varphi}_2$	0.358 (3)	0.262 (8)	0.290 (3)	0.248 (8)
average	0.232	0.160	0.193	0.154

+ 45% + 25% + 4% + 20%

FIG. 7. Physical model of the double pendulum under consideration (a) and the photographic view of the experimental rig (b). Panels (c) and (d) present the stability margin $D(\varphi_2)$ along attractor H calculated for the two sets of excitation parameters [case 1 (c) and case 2 (d)]. Results of experimental investigation are given in the table below. The position of the nozzle is given according to the notation given in Fig. 8. Colors in the table refer to the regions marked with arrows in panels (c) and (d).

phase space around the trajectory. In panels (b)–(d), we show three exemplary basins of attraction calculated for t^1, t^{76}, and t^{114}, respectively. Figure 6(c) presents the basins of attraction calculated for the minimum value of $D_{MIN} = 0.123$ and Fig. 6(d) for the maximum $D_{MAX} = 0.638$.

IV. EXPERIMENTAL RESULTS

Now, we investigate a basic type of a double pendulum, namely, a two degree of freedom system with a harmonic excitation (Fig. 7). The angular displacements of the first and the second pendulum are given by φ_1 and φ_2, respectively. To simplify, both φ_1 and φ_2 are taken from the range $(-\pi, \pi]$ (rad) by applying the modulo function $\varphi_i = [(\varphi_i + \pi) \bmod 2\pi] - \pi$ (rad), for $i = 1, 2$. The rig [Fig. 7(b)] is mounted on the shaker which excites the system parametrically with a harmonic function of the amplitude A_s and frequency ω_s. The horizontal pendulum has the length l_1, mass m_1, moment of inertia J_1, and the center of gravity is located at the distance d_1 from its pin joint. The stiffness of the spring that supports the end of the pendulum is k_1. The second pendulum has the mass m_2, moment of inertia J_2, and the center of gravity is located at d_2 from its pin joint. The viscous damping coefficient in the

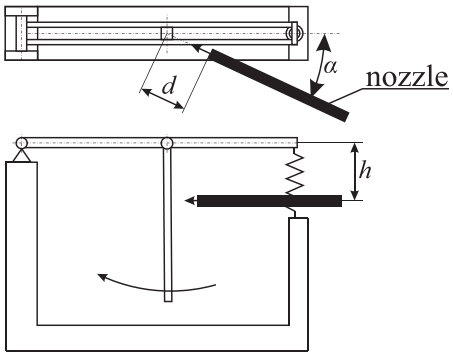

Position no.	d [mm]	h [mm]	α [°]
1	30	35	15
2	30	-35	15
3	30	35	35
4	30	-35	35
5	30	35	105
6	30	-35	105
7	30	35	125
8	30	-35	125

FIG. 8. Nozzle position is given by the angle α and distances d and h. The pair of parameters α and h define the direction of the air flow—consistent (positions: 1, 3, 6, 8) or opposite (positions: 2, 4, 5, 7) to the pendulum linear velocity, while the distance d is constant.

pin joint of the first pendulum is c_1 and of the second one c_2. The dynamics of the system is given by the following set of ODEs:

$$\begin{aligned}&\left(J_2 + m_2 d_2^2\right)\ddot{\varphi}_2 + m_2 d_2\left[A_s\omega_s^2\cos(\omega_s t + t) + g\right]\sin\varphi_2\\&+ m_2 d_2\left\{x_1\left[\cos\left(\varphi_1 - \varphi_2\right)\dot{\varphi}_1^2 + \sin\left(\varphi_1 - \varphi_2\right)\ddot{\varphi}_1\right]\right\}\\&+ c_2\dot{\varphi}_2 = 0, \left(J_1 + m_1 d_1^2 + m_2 x_1^2\right)\ddot{\varphi}_1 + c_1\dot{\varphi}_1\\&+ \frac{1}{2}l_1^2 k_1\sin\left(2\varphi_1\right) + m_2 x_1 d_2\big[\sin\left(\varphi_1 - \varphi_2\right)\ddot{\varphi}_2\\&- \cos\left(\varphi_1 - \varphi_2\right)\dot{\varphi}_2^2\big] + -\left(m_1 d_1 + m_2 x_1\right)\\&\left[A_s\omega_s^2\cos(\omega_s t) + g\right]\cos\varphi_1 = 0.\end{aligned} \tag{7}$$

The parameter values are the following: $J_1 = 4.524 \times 10^{-3}$ (kg m^2), $m_1 = 0.5562$ (kg), $l_1 = 0.315$ (m), $d_1 = 0.180$ (m), $x_1 = 0.153$ (m), $c_1 = 0.05$ (Nm s), $k_1 = 6850$ (N/m), $J_2 = 4.469 \times 10^{-5}$ (kg m^2), $m_2 = 0.02077$ (kg), $d_2 = 0.063$ (m), $c_1 = 7 \times 10^{-6}$ (Nm s), and $g = 9.81$ (m/s^2). All the parameter values were determined in a series of dedicated experiments.[29] In Ref. 5, we have shown stable coexisting periodic solutions for this system and their ranges of stability.

We classify the solutions with respect to the motion of the second pendulum. For validation purposes, we consider the stability of the attractor that refers to 1 : 1 rotations of the second pendulum; we call this solution H. In one period of excitation, the second pendulum performs single rotation and the coordinate φ_2 increases continuously from $-\pi$ (rad) to π (rad). We divide the attractor H into $k = 100$ segments and perform our time-dependent stability margin analysis for two sets of excitation parameters $A_s = 0.002$ (m), $\omega_s = 50$ (rad/s) (case 1) and $A_s = 0.005$ (m), $\omega_s = 35$ (rad/s) (case 2). In case 1, the system has six co-existing solutions, while in case 2 four. For each case, we calculate $m =$ 2 000 000 trials which give us on average 20 000 trials per each considered segment. It is convenient to determine the stability margin with respect to the position of the second pendulum $D(\varphi_2)$. In Figs. 7(c) and 7(d), we present the numerical results obtained for both sets of excitation parameters showing that in both cases, the jump to the other solution is more likely to happen around the upper position of the pendulum. This range is marked with green and purple arrows ($D < 2.25$). The distance to the basin boundary is noticeably larger around $\varphi_2 = 0$, so around the hanging down position, the system is less susceptible for perturbations. With red and blue arrows, we mark the range where $D > 3$.

To validate the proposed method, we perform an experimental investigation using the rig described above. As the source of perturbation, we use a compressor with a controllable pressure and nozzle position. The compressor enables the maximum pressure 0.40 (MPa), and the nozzle has the inner diameter of 4.5 (mm). We investigate eight different positions of the nozzle. In Fig. 8, we present geometrical measures that we use to define the nozzle position, and in the table, we give their values for eight studied positions—each named with the number that is recalled in the results presented in Fig. 7.

We do a series of tests around $\varphi_2 = 0$ (rad) and around $\varphi_2 = \pi$ (rad), each time considering four angles of the nozzle. For each position of the nozzle, we investigate how the perturbations due to the air flow influence the behavior of the pendulum. For each test, we obtain 1 : 1 rotations and start to slowly increase the pressure until we reach the tipping point and the solution changes. To detect this moment precisely, we continuously monitor the period of the pendulum's motion using the optical gate mounted at the bottom frame [see Fig. 7(b)]. For each nozzle position, we perform 10 tests and calculate the average pressure for which the system jumps to the other attractor.

Our results of the experimental tests are given in the table in Fig. 7 and organized to enable a comparison of the results obtained for the same type of perturbations for $\varphi_2 = 0$ (rad) and $\varphi_2 = \pi$ (rad). It is important to remind that the numerically obtained measure D is the distance to the closest boundary of the basins of attraction. Hence, one should not compare the exact values of D with the data in the table which indicates the magnitude of perturbations introduced to the system by the air flow.

The experimental results confirm that around the hanging down position [$\varphi = 0$ (rad)], the system is less susceptible for perturbations. This is somehow predictable but the method can be used for different systems, where the prediction is not so intuitive.

An increase of the average pressure for $\varphi_2 = \pi$ (rad) in comparison to $\varphi_2 = 0$ (rad) is observed in all the considered cases, in particular in case 1, we observe a 45% increase and 25% for case 2. The greater increase for case 1 was also revealed from the numerical analysis [Figs. 7(c) and 7(d)]. Moreover, the experimental results revealed that the difference in the stability margin between both cases is noticeable only around $\varphi_2 = \pi$ (rad) (20% increase), while around

$\varphi_2 = 0$ (rad) it is negligible (4%). This was also deduced with our method [see Figs. 7(c) and 7(d)]. Hence, we obtain a very good correspondence between the experimental data and the numerical predictions. The experimental investigation enabled one to confirm the numerical results and prove the potential practical importance of the proposed method to quantify the stability margin along trajectories.

V. CONCLUSIONS

In this paper, we have presented a novel time-dependent stability measure that enables one to quantify the stability margin along stable periodic orbits. Using this approach, we are able to identify the parts of the orbit, where the system is susceptible for perturbations and assesses the probability of reaching a tipping point.

We present sample-based procedures to get the proposed measures for autonomous and non-autonomous systems. We apply them to paradigmatic models to present the idea and highlight the advantages of the proposed method. Finally, we show an experimental confirmation that the introduced methodology is a reliable tool and expands the knowledge of the dynamics of multistable systems. Moreover, in the proposed method, the algorithm does not become more complex with an increase of system phase space dimensions which is often observed for classical methods (analytical methods, path-following, and basins of attractions).

The proposed new stability measures are especially useful for the analysis of multistable systems and can be utilized to explain more complex dynamics in a wide range of dynamical models in various disciplines of science.

ACKNOWLEDGMENTS

This work is funded by the National Science Center Poland based on the Decision No. DEC-2015/16/T/ST8/00516. We would like to thank Tomasz Kapitaniak, Juliusz Grabski, and Jerzy Wojewoda for support.

[1] S. Auer, F. Hellmann, M. Krause, and J. Kurths, "Stability of synchrony against local intermittent fluctuations in tree-like power grids," Chaos Interdiscip. J. Nonlinear Sci. **27**, 127003 (2017).
[2] S. Auer, K. Kleis, P. Schultz, J. Kurths, and F. Hellmann, "The impact of model detail on power grid resilience measures," Eur. Phys. J. Spec. Top. **225**, 609–625 (2016).
[3] P. Belardinelli and S. Lenci, "A first parallel programming approach in basins of attraction computation," Int. J. Non Linear Mech. **80**, 76–81 (2016).
[4] P. Brzeski, M. Lazarek, T. Kapitaniak, J. Kurths, and P. Perlikowski, "Basin stability approach for quantifying responses of multistable systems with parameters mismatch," Meccanica **51**, 2713–2726 (2016).
[5] P. Brzeski, J. Wojewoda, T. Kapitaniak, J. Kurths, and P. Perlikowski, "Sample-based approach can outperform the classical dynamical analysis-experimental confirmation of the basin stability method," Sci. Rep. **7**, 6121 (2017).
[6] T. Coletta, R. Delabays, I. Adagideli, and P. Jacquod, "Topologically protected loop flows in high voltage AC power grids," New J. Phys. **18**, 103042 (2016).
[7] A. Daza, A. Wagemakers, B. Georgeot, D. Guéry-Odelin, and M. A. F. Sanjuán, "Basin entropy: A new tool to analyze uncertainty in dynamical systems," Sci. Rep. **6**, 31416 (2016).
[8] A. Daza, B. Georgeot, D. Guéry-Odelin, A. Wagemakers, and M. A. F. Sanjuán, "Chaotic dynamics and fractal structures in experiments with cold atoms," Phys. Rev. A **95**, 013629 (2017).
[9] R. de la Llave, "A tutorial on KAM theory," in *Proceedings of Symposia in Pure Mathematics 69*, edited by A. Katok *et al.* (American Mathematical Society, 2001), pp. 175–292.
[10] E. Eschenazi, H. G. Solari, and R. Gilmore, "Basins of attraction in driven dynamical systems," Phys. Rev. A **39**, 2609 (1989).
[11] H. Fang and K. W. Wang, "Piezoelectric vibration-driven locomotion systems—exploiting resonance and bistable dynamics," J. Sound Vib. **391**, 153–169 (2017).
[12] J. Huang and A. C. J. Luo, "Analytical solutions of period-1 motions in a buckled, nonlinear Jeffcott rotor system," Int. J. Dyn. Control **4**, 376–383 (2016).
[13] G. Iooss and D. D. Joseph, *Elementary Stability and Bifurcation Theory* (Springer Science & Business Media, Berlin, 2012).
[14] Y.-B. Kim, "Quasi-periodic response and stability analysis for non-linear systems: A general approach," J. Sound Vib. **192**, 821–833 (1996).
[15] H. Kim, S. H. Lee, and P. Holme, "Community consistency determines the stability transition window of power-grid nodes," New J. Phys. **17**, 113005 (2015).
[16] H. Kim, S. H. Lee, and P. Holme, "Building blocks of the basin stability of power grids," Phys. Rev. E **93**, 062318 (2016).
[17] V. Kohar, P. Ji, A. Choudhary, S. Sinha, and J. Kurths, "Synchronization in time-varying networks," Phys. Rev. E **90**, 022812 (2014).
[18] Y. Kuznetsov, *Elements of Applied Bifurcation Theory* (Springer-Verlag, New York, 1995).
[19] A. N. Lansbury, J. M. T. Thompson, and H. B. Stewart, "Basin erosion in the twin-well duffing oscillator: Two distinct bifurcation scenarios," Int. J. Bifurcat. Chaos **2**, 505–532 (1992).
[20] S. Lenci and G. Rega, "Competing dynamic solutions in a parametrically excited pendulum: Attractor robustness and basin integrity," J. Comput. Nonlinear Dyn. **3**, 041010 (2008).
[21] S. Lenci and G. Rega, "Experimental versus theoretical robustness of rotating solutions in a parametrically excited pendulum: A dynamical integrity perspective," Physica D **240**, 814–824 (2011).
[22] S. Leng, W. Lin, and J. Kurths, "Basin stability in delayed dynamics," Sci. Rep. **6**, 21449 (2016).
[23] O. V. Maslennikov, V. I. Nekorkin, and J. Kurths, "Basin stability for burst synchronization in small-world networks of chaotic slow-fast oscillators," Phys. Rev. E **92**, 042803 (2015).
[24] P. J. Menck, J. Heitzig, N. Marwan, and J. Kurths, "How basin stability complements the linear-stability paradigm," Nat. Phys. **9**, 89–92 (2013).
[25] C. Mitra, J. Kurths, and R. V. Donner, "An integrative quantifier of multistability in complex systems based on ecological resilience," Sci. Rep. **5**, 16196 (2015).
[26] G. Rega and S. Lenci, "Identifying, evaluating, and controlling dynamical integrity measures in non-linear mechanical oscillators," Nonlinear Anal. Theory Methods Appl. **63**, 902–914 (2005).
[27] B. Schäfer, C. Grabow, S. Auer, J. Kurths, D. Witthaut, and M. Timme, "Taming instabilities in power grid networks by decentralized control," Eur. Phys. J. Spec. Top. **225**, 569–582 (2016).
[28] P. Schultz, J. Heitzig, and J. Kurths, "Detours around basin stability in power networks," New J. Phys. **16**, 125001 (2014).
[29] J. Strzalko, J. Grabski, J. Wojewoda, M. Wiercigroch, and T. Kapitaniak, "Synchronous rotation of the set of double pendula: Experimental observations," Chaos Interdiscip. J. Nonlinear Sci. **22**, 047503 (2012).
[30] J. M. T. Thompson, "Chaotic phenomena triggering the escape from a potential well," Proc. R. Soc. Lond. A **421**, 195–225 (1989).
[31] J. M. T. Thompson and M. S. Soliman, "Fractal control boundaries of driven oscillators and their relevance to safe engineering design," Proc. R. Soc. Lond. A **428**, 1–13 (1990).
[32] J. A. Yorke and H. E. Nusse, *Dynamics: Numerical Explorations* (Springer-Verlag, New York, 1998).
[33] Y. Zou, T. Pereira, M. Small, Z. Liu, and J. Kurths, "Basin of attraction determines hysteresis in explosive synchronization," Phys. Rev. Lett. **112**, 114102 (2014).